

Redox freezing and melting in the Earth's deep mantle resulting from carbon–iron redox coupling

Arno Rohrbach¹ & Max W. Schmidt¹

Very low seismic velocity anomalies in the Earth's mantle^{1,2} may reflect small amounts of melt present in the peridotite matrix, and the onset of melting in the Earth's upper mantle is likely to be triggered by the presence of small amounts of carbonate³. Such carbonates stem from subducted oceanic lithosphere in part buried to depths below the 660-kilometre discontinuity and remelted into the mantle. Here we demonstrate that carbonate-induced melting may occur in deeply subducted lithosphere at near-adiabatic temperatures in the Earth's transition zone and lower mantle. We show experimentally that these carbonatite melts are unstable when infiltrating ambient mantle and are reduced to immobile diamond when recycled at depths greater than ~250 kilometres, where mantle redox conditions are determined by the presence of an (Fe,Ni) metal phase^{4–6}. This 'redox freezing' process leads to diamond-enriched mantle domains in which the Fe⁰, resulting from Fe²⁺ disproportionation in perovskites and garnet, is consumed but the Fe³⁺ preserved. When such carbon-enriched mantle heterogeneities become part of the upwelling mantle, diamond will inevitably react with the Fe³⁺ leading to true carbonatite redox melting at ~660 and ~250 kilometres depth to form deep-seated melts in the Earth's mantle.

The Earth's mantle is a heterogeneous, marble-cake-like composite of pristine, depleted, and mostly pyroxenitic or eclogitic recycled material^{7,8}, further complicated by heterogeneities left behind in ancient melt passageways (for example, dunites, cumulative pyroxenites, or carbon-enriched domains formed through redox freezing). These heterogeneities are different from average mantle in terms of bulk composition⁷, or formed through differences in H₂O or CO₂ volatile influx. Melting processes in the deep mantle are triggered by such heterogeneities, as solidus temperatures for fertile or depleted peridotite are significantly higher than adiabatic temperatures at depths >120 km. Using high pressure experiments, we investigate the formation of C-enriched mantle domains in the vicinity of deeply subducted lithosphere (through redox reactions between recycled carbonate and ambient metal-bearing mantle) and the remelting of such domains when entrained into the convective mantle.

Carbonated peridotite systems are central to understanding processes that involve the recycling of subducted, carbonated lithosphere back into the mantle. Experiments have shown that at pressures above ~2.5 GPa, carbonated mantle melts at lower temperatures than carbonate-free mantle^{3,9–12}. However, these experimental studies have maintained carbon in its oxidized form. To understand what happens within the generally reduced deep Earth, it is necessary to include redox equilibria (controlled by oxygen fugacity, f_{O_2}) between intrinsically oxidized carbonate minerals or melts and the reduced and metal-bearing deep mantle.

The redox state of the mantle determines whether carbon is present in its oxidized and potentially mobile form as carbonate or carbonatite melt (which lower the mantle solidus by several hundred degrees^{3,9–12}), or whether it is present in its reduced and immobile form as graphite or diamond (which do not affect melting temperatures). In the uppermost mantle to ~250 km depth, f_{O_2} is determined by Fe²⁺/Fe³⁺ equilibria in silicate minerals. Studies of natural peridotite xenoliths show

that mantle f_{O_2} decreases with increasing pressure¹³, such that carbonates or carbonatites are not stable at depths greater than ~120 km in subcratonic and asthenospheric mantle^{14,15}. Fe²⁺/Fe³⁺ equilibria in a predominantly magnesian mantle are inefficient in buffering f_{O_2} because slight changes in the Fe²⁺/Fe³⁺ ratio have a strong impact on mantle f_{O_2} (ref. 16). Oxygen fugacity in the upper mantle is thus affected by processes such as partial melting, mantle metasomatism, and recycling of oxidized material by subduction. Small amounts of admixed oxidized component may raise the f_{O_2} of a limited mantle domain such that carbonates become stable and f_{O_2} is controlled by equilibria like enstatite + magnesite = olivine + graphite/diamond (EMOG/EMOD)¹⁷. The onset of carbonatite melting depends then solely on the solidus of carbonated peridotite.

This situation changes at higher pressures: thermodynamic calculations⁴ and experiments^{5,6,18} demonstrate that f_{O_2} decreases with increasing pressure such that (Fe,Ni)-metal probably becomes stable at ~250 km depth^{6,14} and in all mantle regions below⁵. At metal saturation depths, f_{O_2} in the Earth's mantle becomes narrowly constrained. Given equilibrium between mantle phases with molar Mg/(Mg+Fe²⁺) (= X_{Mg}) ≈ 0.90 and (Fe,Ni) metal, f_{O_2} can only vary from values around the iron–wüstite (IW) equilibrium where the metal would be Ni-rich, to about 1.5 logarithmic units below IW where the metal would be almost pure iron. Because these equilibria have a considerable buffer capacity and the mantle represents an almost infinite reservoir, the mantle is capable of imposing its ambient f_{O_2} on any additional redox sensitive component, such as carbonates, carbonatites or carbon–hydrogen–oxygen fluids. Redox state differences between such fluids and ambient peridotite may trigger local hydrous redox melting¹⁹ at shallow mantle depths when fluid speciation changes from reduced methane-rich to oxidized water-rich.

At larger mantle depths, small amounts of H₂O can be incorporated into nominally anhydrous minerals^{20,21} and CO₂ dominates the lowering of melting temperatures through volatiles²². To explore whether redox equilibria involving recycled carbonates trigger the deepest melting in the Earth's mantle, we investigated a carbonated fertile mantle at pressures (10–23 GPa), temperatures (1,400–1,900 °C) and redox conditions relevant for the mid-upper to lower mantle using high-pressure multianvil devices (Methods).

The first set of experiments constrains the solidus of a carbonated fertile peridotite at 10, 14 and 23 GPa to temperatures of 1,535, 1,600 and 1,675 °C (Fig. 1). Melting temperatures determined previously vary considerably, mainly because of variations in the bulk alkali contents and the use of synthetic analogues^{3,9–12}. Our 10 GPa solidus temperature corresponds well to the ~1,500 °C reported previously for 10 GPa in a study on natural carbonated peridotite³, and thus provides a direct link between our data set and lower-pressure data. The solidus from 10 to 23 GPa proceeds parallel to that of alkali-enriched peridotite at 10–20 GPa (ref. 10), although absolute temperatures obtained with our composition are 100–150 °C higher (Fig. 1). This difference results from our considerably lower, peridotite-like, alkali content and a therefore lower alkali/CO₂ ratio (0.06 this study; 0.18 in ref. 10), which is potentially a key variable controlling solidus temperatures³.

¹Institut für Geochemie und Petrologie, ETH Zürich, Sonneggstrasse 5, 8092 Zürich, Switzerland.

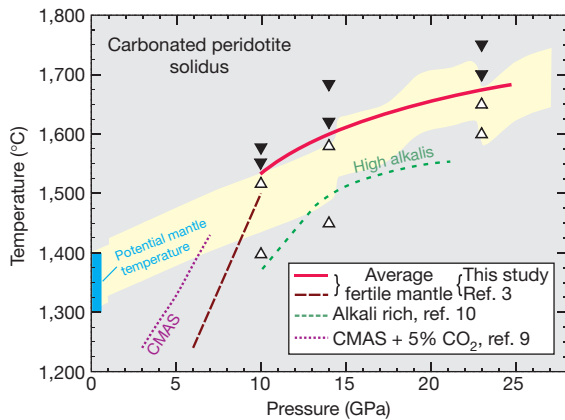


Figure 1 | The solidus of carbonated peridotite. Solid red line, solidus as bracketed by our experiments. Subsolidus runs, open triangles; runs containing carbonatite melt, filled inverted triangles. Run pressure uncertainties are smaller than symbol size; for temperature uncertainties see Methods. Dashed lines, solidus of natural peridotite; dotted line, solidus of a synthetic $\text{CaO-MgO-Al}_2\text{O}_3\text{-SiO}_2$ (CMAS) + CO_2 analogue system⁹. Brown long-dashed line, natural peridotite + 2.5 wt% CO_2 (ref. 3); green short-dashed line, natural peridotite + 5 wt% CO_2 enriched with 0.5 wt% Na_2O + 0.4 wt% K_2O (ref. 10). Solidi temperatures decrease with increasing bulk alkali/ CO_2 ratio³, although K appears to have a much stronger effect than Na (compare refs 3 and 10 with similar alkali/ CO_2). Blue bar, range of potential mantle temperatures at 1 bar extrapolated to depth (yellow corridor) assuming adiabatic behaviour in a convecting mantle³². The solidus of carbonated peridotite approaches the geotherm at ~ 10 GPa (ref. 3). As at higher pressures the solidus continues within the range of adiabatic temperatures, we suggest that carbonatitic melts may form at ambient mantle temperatures over a large pressure interval if carbonate is stable with respect to f_{O_2} .

The steep positive slope of the solidus in a pressure–temperature (P – T) plot— 55°C per GPa up to 10 GPa (ref. 3)—changes between 10 and 15 GPa to a rather weak temperature dependence of 12°C per GPa at >15 GPa. We attribute this change to an increase in activity with pressure of mainly Na_2O but also CaO , caused by the continuous decrease in modal abundance of clinopyroxene. Above 15 GPa, pyroxene completely dissolves in majorite–garnet solid solution²³. Sodium is relatively incompatible in the garnet structure and partitions strongly into a carbonatite liquid, thus causing relatively low melting temperatures. The solidus of carbonated peridotite approaches the mantle geotherm at about 10 GPa and from then on remains close to ambient adiabatic mantle temperatures (Fig. 1). Carbonatite melting in the deep Earth’s mantle does therefore not require anomalously high temperatures and carbonatites may be produced over large depth intervals.

In two further series of experiments, we determined carbon speciation as a function of f_{O_2} for slightly subadiabatic mantle temperatures. For this, we first equilibrated the carbonated peridotite with Fe–FeO, Ni–NiO, (Ni,Au)–NiO and Re– ReO_2 solid state metal–metal oxide buffers at 14 GPa, 1,450 °C and 23 GPa, 1,600 °C. Fe, Ni, Ni–Au and Re metal were used as capsule materials, and the respective oxide was either contained in the starting material, or (in the case of ReO_2) added to the charge. Oxygen fugacities imposed by these buffers range from -1 to $+5$ log units relative to IW (Methods). Experiments under oxidizing conditions (IW +4 to +5) in Re and Au–Ni capsules yield almost pure magnesite ($X_{\text{Mg}} = 0.96$), whereas runs in Fe and Ni capsules reveal that carbonate is not stable at $f_{\text{O}_2} < \text{IW} + 1.2$ at either 14 or 23 GPa (Fig. 2). Instead, carbonate is reduced to micrometre-sized diamonds, identified in backscatter electron images and measured using energy-dispersive spectroscopy. Elevated FeO and NiO contents and fractions in the minerals provide further evidence for carbonate reduction via



where (Fe,Ni,Mg)O is a compound in olivine, garnet and perovskite or is ferropericlase.

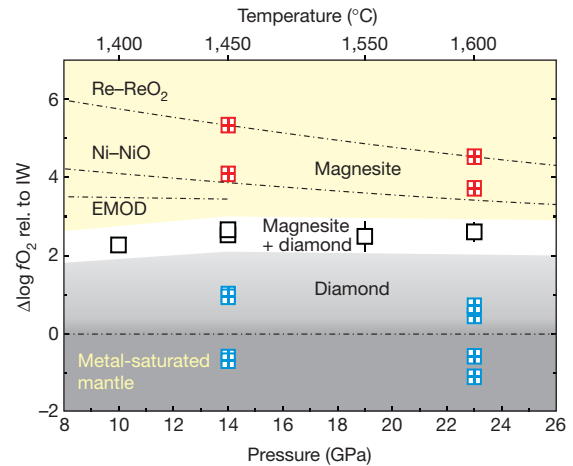


Figure 2 | Carbon speciation in natural mantle as a function of pressure, temperature and f_{O_2} . Plotted are calculated log f_{O_2} values relative to the IW reference (Methods) for magnesite-bearing runs (red symbols), diamond-bearing runs (blue symbols) and runs containing diamond + magnesite using Ir as redox sensor (black symbols). Coloured areas mark the stability fields of magnesite (yellow), magnesite+diamond (white) and diamond (light grey). Run durations were at least 24 h to ensure redox equilibrium between the phases (Supplementary Table 1). The stability field of magnesite remains at ≥ 2 log units above IW up to 23 GPa; no strong pressure dependence is evident from our data. At the low f_{O_2} conditions estimated for the Earth’s mantle which lead to metal saturation at pressures higher than ~ 8 GPa (corresponding to ~ 250 km depths; dark grey area), carbonates and carbonatites are unstable and will be reduced to diamond according to reaction (1). Relative positions of IW and Ni–NiO buffers calculated after ref. 33; for relative position of Re– ReO_2 , see Methods. The EMOD buffer dominating in the uppermost mantle¹⁷ (equation given in the text) is limited to ~ 14 GPa by the stability of olivine and pyroxene. Run pressure uncertainties are within the size of the symbols, as are propagated 2σ errors for f_{O_2} unless error bars are reported. Errors include analytical uncertainties and 2σ standard deviations from averages for runs where f_{O_2} was calculated for multiple phases separately, but do not include uncertainties of the activity models which are difficult to quantify. Because of this, we suggest that an additional uncertainty for all f_{O_2} values reported is ± 0.3 log units.

Additionally, we monitored f_{O_2} in experiments saturated in both diamond and carbonate at 10–23 GPa by adding 5 wt% iridium metal as a redox sensor²⁴. The Fe content in Ir, together with the FeO content in silicates or oxides, allows the calculation of f_{O_2} conditions during the experiment (Methods). The carbonated peridotite was saturated with elemental carbon through the use of graphite capsules that transformed to diamond or, for noble metal capsules, through addition of 10 wt% C. We also added 3 wt% Fe^0 to enhance the mass reacted through equilibrium (1). These redox sensing experiments yield f_{O_2} values slightly lower than calculated for the EMOD equilibrium at 10 and 14 GPa and then remain rather constant at 2.3–2.7 log units above IW up to 23 GPa. This is consistent with the f_{O_2} corridor between IW +1.2 to +4, as defined by the externally buffered experiments, in which the coexistence of diamond+diamond would be possible (Fig. 2).

Our results imply that at an ambient, fertile mantle f_{O_2} around IW – 1.5 (ref. 14), carbonate that is remixed into the mantle at >250 km depth is unstable and will be reduced to diamond. Typical carbon concentrations of 20–250 p.p.m. C for sub-ridge mantle (ref. 25 and references therein) would inevitably dissolve in the metal phase present at these depths or form discrete iron carbides, like Fe_3C and Fe_7C_3 , depending on Fe–C ratio and P – T conditions^{25,26}. Thus, carbonate related melting is unlikely to occur in Earth’s lower mantle, the transition zone and the lowermost upper mantle as long as sub-ridge carbon concentrations prevail (Fig. 2). Although the mantle ceases to be metal saturated in shallower parts of the upper mantle (<250 km, ref. 6), the average f_{O_2} up to 100–150 km depth presumably remains too low to sustain carbonates or carbonatites as equilibrium phases at sub-ridge carbon concentrations¹⁵.

However, the addition of subducted carbonate to average mantle fundamentally changes this behaviour. Relative buffer capacity changes in the Earth's mantle induce immobilization of carbonatite melts through 'redox freezing', that is, reduction of carbonatites to diamond, as well as remobilization of carbon through redox melting. Redox melting transforms diamond to carbonatite melts, which potentially control the onset of ultra-deep melting. Starting from a subducting, locally carbonated, relatively oxidized mafic to ultramafic lithosphere, our experiments demonstrate that carbonatite melts will be generated in such lithosphere on thermal relaxation (Fig. 1). This may occur when the lithosphere deflects into the transition zone above the 660-km discontinuity or when stagnating in the lower mantle. On a local scale, oxidized carbonatite melt migrating into the mantle will consume metal to first form iron carbide in an intermittent stage, and then further oxidize the Fe and Ni contained in the carbide to leave a mantle domain that contains all iron as Fe^{2+} and Fe^{3+} in silicates and ferropicrinite and all carbon as diamond. Owing to its low viscosity and high wetting properties^{27,28}, any excess carbonatite not consumed by redox reactions would percolate upwards along grain boundaries and exhaust further (Fe,Ni)-metal and carbide until complete redox freezing—that is, immobilization due to reduction of CO_2 to C^0 —is achieved. This presumably very efficient process will eventually exhaust all buffering metal and carbide through precipitation of diamond, and result in a metal-free mantle domain where diamond coexists with Fe^{3+} -bearing garnet or perovskite (Fig. 3).

At the boundary of such domains, where the supply of carbonatite melt does not exceed the redox capacity of Fe,Ni-metal, an iron carbide rim is expected to form. The redox capacity of Fe^{3+} in such mantle domains would be exactly equivalent or slightly superior (due to the Fe^{3+} present before disproportionation of Fe^{2+}) to that necessary to re-convert all diamond to CO_2 . Similarly, the maximum increase in C content of mantle domains metasomatized by carbonatites derived from the subducting lithosphere is restricted to $\sim 1,000$ p.p.m., equivalent to the amount of carbonatite that may be immobilized by the maximum Fe-metal content of 1 wt% expected in the lower mantle⁵.

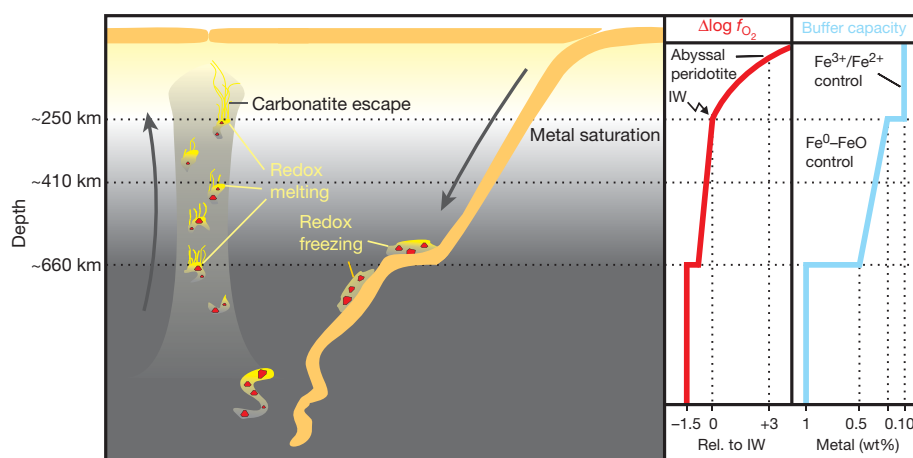


Figure 3 | Carbonatitic redox freezing and redox melting caused by redox capacity changes in Earth's mantle. Main panel, cartoon illustrating a possible sequence of redox freezing and redox melting events driven by oxidation state contrasts between subducted lithosphere and ambient asthenospheric mantle. Right, potential mantle f_{O_2} (red line) and redox buffer capacity (blue line) as function of depth. f_{O_2} decreases in the subcratonic upper mantle¹³ to reach \sim IW and metal saturation at ~ 250 km depth^{6,14}. Change in redox control from $\text{Fe}^{2+}/\text{Fe}^{3+}$ in the upper mantle to Fe^0 -FeO provides a considerable gain in f_{O_2} buffer capacity. At >250 km depth, the mantle and all redox sensitive components are bound to f_{O_2} levels $<$ IW unless all metal is exhausted. Majoritic garnet in equilibrium with Fe^0 incorporates more Fe^{3+} with increasing pressure⁶; adequate charge balance results from reduction of FeO to Fe^0 which increases the Fe^0 metal abundance. An estimate yields 0.5 wt% metal at the base of the transition zone, assuming all Ni is present as Ni^0 (1,800 p.p.m.)

As the metal content is expected to decrease with decreasing pressure (Fig. 3), the corresponding maximum C content of metasomatized domains would also be lower for domains formed at shallower depth.

The inverse process, redox melting, would occur when such mantle heterogeneities are entrained by upwelling mantle and cross the 660-km discontinuity and transition zone. Destabilization of Fe^{3+} -rich perovskite without an adequate amount of Fe^0 for comproportionation (the opposite process to disproportionation) inevitably leads to a sudden increase in Fe^{3+} activity at the 660-km discontinuity and thus to the re-oxidation of diamond to CO_2 . This redox reaction would directly result in carbonatite melts within upwelling, previously melt-free but diamond-bearing mantle. Carbonatitic redox melting might also explain the virtual absence of pyrolytic mineral inclusions in diamonds originating from sublithospheric depths (>200 – 300 km)²⁹. Pyrolytic pristine mantle itself does not contain sufficient C to form diamonds²⁵, and thus diamonds are expected to form dominantly through the above redox freezing process wherever carbonatites percolate. The inverse process—that is, redox melting which destroys most of these diamonds through oxidation—then leads to the generation of melts that carry remnants of such deep mantle domains to the Earth's surface. Average mantle is expected to contain ~ 1 wt% Fe^0 formed from Fe^{2+} disproportionation in the lower mantle⁵; such metal fractions are stable and would not segregate to Earth's core³⁰. For reaction (1), the redox capacity of 1 wt% Fe^0 is equivalent to 0.8 wt% magnesite. As argued above, the properties of carbonatite melt result in a self-regulating mechanism, where infiltrating carbonatite melt oxidizes all Fe^0 , leaving behind a diamond-bearing mantle domain with exactly the same redox-capacity (that is, that of 0.8 wt% magnesite). In the reverse process, it can thus be expected that about 1 wt% of carbonatite melt forms in such upwelling mantle domains. Although upwelling occurs at speeds comparable to plate tectonic movements (that is, 1 – 10 cm yr^{-1}), 1% low viscosity melt in the mantle matrix rises with speeds of at least 10 – 100 m yr^{-1} (ref. 31). Consequently, carbonatite flow will tend to escape from the upwelling mantle matrix but will suffer redox freezing as long as progressing carbonatite melts encounter

plus $\sim 3,200$ p.p.m. Fe^0 calculated from mass balance (mantle: 8 wt% $\text{FeO}^{\text{total}}$, 40 vol% majoritic garnet: 5.5 wt% $\text{FeO}^{\text{total}}$, $\text{Fe}^{3+}/\Sigma\text{Fe} = 0.33$ (ref. 6); 60 vol% ringwoodite: 9.7 wt% $\text{FeO}^{\text{total}}$, $\text{Fe}^{3+}/\Sigma\text{Fe} = 0.02$ (ref. 14)). Transition to the lower mantle is accompanied by a gain in buffer capacity because MgSi-perovskite incorporates more Fe^{3+} at metal saturation f_{O_2} than majoritic garnet, resulting in ~ 1.0 wt% metal⁵. Remixing of subducted carbonated lithosphere into the mantle at these depths leads to redox freezing and diamond-enriched mantle domains. Domains incorporated into upwelling mantle will experience redox melting, most prominently at levels where the capacity of the mantle phases to incorporate Fe^{3+} changes drastically, that is, at ~ 660 km and ~ 250 km depth. Melts produced from C-enriched domains cannot escape through the surrounding metal-bearing average mantle, but will freeze until redox control shifts from metal saturation back to bulk $\text{Fe}^{2+}/\text{Fe}^{3+}$ controlled at ~ 250 m depth.

metal-bearing mantle. It is only at depths <250 km when garnet becomes less majoritic, Fe^{3+} activity increases, and the mantle ceases to be metal-saturated, that this scenario changes. At this depth, f_{O_2} buffering in the mantle shifts back from being controlled by $\text{Fe}^0/\text{Fe}^{2+}$ to being controlled by $\text{Fe}^{2+}/\text{Fe}^{3+}$, which leads to a dramatic decline in buffering capacity. Such mantle has little potential to hinder carbonatite melts from percolating upwards.

We expect that redox equilibria control the formation of deep carbonatite melts, and that at ~250 km depth a continuous flow of carbonatite melt originating from mantle heterogeneities may form in upwelling mantle, which is probably reflected in seismic low velocity anomalies^{1,2} observed at these depths. If melt quantities are too low and evade direct seismological observation, their presence may be confirmed by enhanced electrical conductivity or seismic anisotropies caused by matrix reorganization³.

METHODS SUMMARY

Starting composition. The starting composition for the experiments represents a fertile peridotite enriched in 5 wt% CO_2 . NiO in this composition was set to 1 wt%, to ensure that the NiO content of the phases was high enough for microprobe analysis and f_{O_2} calculations. Experiments using Ir as a redox sensor were without Ni to ensure that the metal is a binary Fe–Ir alloy.

Oxygen fugacity calculations. We calculate f_{O_2} using Fe–FeO and Ni–NiO redox equilibria. f_{O_2} values are reported relative to iron–wüstite (IW), nickel–NiO (NNO) and rhenium– ReO_2 (RRO), using activity–composition relationship for (Fe,Ni) alloys and (Au,Ni) alloys (Methods). f_{O_2} values of ferropericlase (fp)-bearing experiments are calculated from



with $\text{M} = \text{Fe}$ or Ni . f_{O_2} relative to the respective metal–metal oxide (MMO) equilibrium is given by

$$\Delta \log f_{\text{O}_2} [\text{MMO}] = 2 \log a_{\text{MO}}^{\text{fp}} - 2 \log a_{\text{M}}^{\text{metal}} \quad (3)$$

where activity a is defined as molar fraction X times activity coefficient γ . f_{O_2} conditions of runs containing olivine, wadsleyite or ringwoodite were calculated from Fe activity in the olivine polymorph and the coexisting metal phase using binary symmetric solution models for activity corrections.

Iridium redox sensing. Ir metal was used as a redox sensor²⁴ to determine f_{O_2} in runs containing elemental carbon+magnesite. Margules interaction parameters were obtained by least-squares fitting of a binary asymmetric regular solution model to X-ray data for face-centred cubic (f.c.c.) Ir–Fe alloy (Methods). Activity coefficients γ , dependent on P , T and X for Fe in f.c.c. Ir–Fe alloy, are given by

$$RT \ln(\gamma_{\text{Fe}}) = 2X_{\text{Fe}}X_{\text{Ir}}W_{\text{G Ir-Fe}} + X_{\text{Ir}}^2W_{\text{G Fe-Ir}} - 2G^{\text{XS}} \quad (4)$$

with G^{XS} being the excess Gibbs free energy of mixing, and $W_{\text{G Ir-Fe}}$, $W_{\text{G Fe-Ir}}$ being the Margules parameters. Correcting the activity model for P and T is described in Methods and shown in Supplementary Fig. 1.

Full Methods and any associated references are available in the online version of the paper at www.nature.com/nature.

Received 28 May 2010; accepted 31 January 2011.

Published online 23 March 2011.

1. Forsyth, D. W. *et al.* Imaging the deep seismic structure beneath a mid-ocean ridge: the MELT experiment. *Science* **280**, 1215–1218 (1998).
2. Gu, Y. J., Lerner-Lamb, A. L., Dziewonski, A. M. & Ekström, G. Deep structure and seismic anisotropy beneath the East Pacific Rise. *Earth Planet. Sci. Lett.* **232**, 259–272 (2005).
3. Dasgupta, R. & Hirschmann, M. M. Melting in the Earth's deep upper mantle caused by carbon dioxide. *Nature* **440**, 659–662 (2006).
4. Ballhaus, C. Is the upper mantle metal-saturated? *Earth Planet. Sci. Lett.* **132**, 75–86 (1995).
5. Frost, D. J. *et al.* Experimental evidence for the existence of iron-rich metal in the Earth's lower mantle. *Nature* **428**, 409–412 (2004).
6. Rohrbach, A. *et al.* Metal saturation in the upper mantle. *Nature* **449**, 456–458 (2007).

7. Allègre, C. J. & Turcotte, D. L. Implications of a two-component marble-cake mantle. *Nature* **323**, 123–127 (1986).
8. Hofmann, A. W. Mantle geochemistry: the message from oceanic volcanism. *Nature* **385**, 219–229 (1997).
9. Dalton, J. A. & Presnall, D. C. Carbonatitic melts along the solidus of model lherzolite in the system $\text{CaO-MgO-Al}_2\text{O}_3\text{-SiO}_2\text{-CO}_2$ from 3 to 7 GPa. *Contrib. Mineral. Petrol.* **131**, 123–135 (1998).
10. Ghosh, S., Ohtani, E., Litasov, K. D. & Terasaki, H. Solidus of carbonated peridotite from 10 to 20 GPa and origin of magnesio-carbonatite melt in the Earth's deep mantle. *Chem. Geol.* **262**, 17–28 (2009).
11. Brey, G. P., Bulatov, V. K., Gurnis, A. V. & Lahaye, Y. Experimental melting of carbonated peridotite at 6–10 GPa. *J. Petrol.* **49**, 797–821 (2008).
12. Litasov, K. D. & Ohtani, E. Solidus and phase relations of carbonated peridotite in the system $\text{CaO-Al}_2\text{O}_3\text{-MgO-SiO}_2\text{-Na}_2\text{O-CO}_2$ to the lower mantle depths. *Phys. Earth Planet. Inter.* **177**, 46–58 (2009).
13. Woodland, A. B. & Koch, M. Variation in oxygen fugacity with depth in the upper mantle beneath the Kaapvaal craton, South Africa. *Earth Planet. Sci. Lett.* **214**, 295–310 (2003).
14. Frost, D. J. & McCammon, C. A. The redox state of the Earth's mantle. *Annu. Rev. Earth Planet. Sci.* **36**, 389–420 (2008).
15. Stagno, V. & Frost, D. J. Carbon speciation in the asthenosphere: experimental measurements of the redox conditions at which carbonate-bearing melts coexist with graphite or diamond in peridotite assemblages. *Earth Planet. Sci. Lett.* **300**, 72–84 (2010).
16. Gudmundsson, G. & Wood, B. J. Experimental tests of garnet peridotite oxygen barometry. *Contrib. Mineral. Petrol.* **119**, 56–67 (1995).
17. Egglar, D. H. & Baker, D. R. in *High Pressure Research in Geophysics* (eds Akimoto, S. & Manghni, M. H.) 237–250 (Centre for Academic Publishing, 1982).
18. O'Neill, H. St C. *et al.* in *Evolution of the Earth and Planets* (eds Takahashi, E., Jeanloz, R. & Rubie, D. C.) 73–88 (Geophys. Monogr. 74, Int. Union Geol. Geophys./Am. Geophys. Union, 1993).
19. Taylor, W. R. & Green, D. H. in *Magmatic Processes and Physicochemical Principles* (ed. Mysen, B. O.) 121–138 (Spec. Publ. No. 1, Geochem. Soc. USA, 1987).
20. Kohn, S. C. Solubility of H_2O in nominally anhydrous mantle minerals using ^1H MAS NMR. *Am. Mineral.* **81**, 1523–1526 (1996).
21. Keppler, H. & Bolfan-Casanova, N. in *Water in Nominally Anhydrous Minerals* (eds Keppler, H. & Smyth, J. R.) 193–230 (Reviews in Mineralogy and Geochemistry 62, Min. Soc. Am., 2006).
22. Luth, R. W. in *Mantle Petrology: Field Observations and High Pressure Experimentation: A Tribute to Francis R. (Joe) Boyd* (eds Fei, Y., Bertka, C. M. & Mysen, B. O.) 297–316 (Geochemical Society, 1999).
23. Ringwood, A. E. The pyroxene–garnet transformation in the Earth's mantle. *Earth Planet. Sci. Lett.* **2**, 255–263 (1967).
24. Woodland, A. B. & O'Neill, H. St C. Thermodynamic data for Fe-bearing phases obtained using noble metal alloys as redox sensors. *Geochim. Cosmochim. Acta* **61**, 4359–4366 (1997).
25. Dasgupta, R. & Hirschmann, M. M. The deep carbon cycle and melting in Earth's interior. *Earth Planet. Sci. Lett.* **298**, 1–13 (2010).
26. Lord, O. T., Walter, M. J., Dasgupta, R., Walker, D. & Clark, S. M. Melting in the Fe–C system to 70 GPa. *Earth Planet. Sci. Lett.* **284**, 157–167 (2009).
27. Minarik, W. G. & Watson, E. B. Interconnectivity of carbonate melt at low melt fraction. *Earth Planet. Sci. Lett.* **133**, 423–437 (1995).
28. Hunter, R. H. & McKenzie, D. The equilibrium geometry of carbonate melts in rocks of mantle composition. *Earth Planet. Sci. Lett.* **92**, 347–356 (1989).
29. Stachel, T., Brey, G. P. & Harris, J. W. Inclusions in sublithospheric diamonds: glimpses of deep earth. *Elements* **1**, 73–78 (2005).
30. Bagdassarov, N., Solferino, G., Golabek, G. J. & Schmidt, M. W. Centrifuge assisted formation of Fe–S melts in partially molten peridotite: time constraints for planetary core formation. *Earth Planet. Sci. Lett.* **288**, 84–95 (2009).
31. Connolly, J. A. D., Schmidt, M. W., Solferino, G. & Bagdassarov, N. Permeability of asthenospheric mantle and melt extraction rates at mid-ocean ridges. *Nature* **462**, 209–212 (2009).
32. Stixrude, L. & Lithgow-Bertelloni, C. Influence of phase transformations on lateral heterogeneity and dynamics in Earth's mantle. *Earth Planet. Sci. Lett.* **263**, 45–55 (2007).
33. Campbell, A. J. *et al.* High pressure effects on the iron–iron oxide and nickel–nickel oxide oxygen fugacity buffers. *Earth Planet. Sci. Lett.* **286**, 556–564 (2009).

Supplementary Information is linked to the online version of the paper at www.nature.com/nature.

Acknowledgements Discussions with P. Ulmer, U. Mann and C. Ballhaus stimulated this work. Comments and suggestions from T. Stachel improved the manuscript. Financial support by Swiss National Science Foundation (SNSF) grant 2-777-86-06 is acknowledged.

Author Contributions M.W.S. and A.R. designed this project and M.W.S. obtained its funding. Experiments, analytical work and f_{O_2} calculations were done by A.R.; both authors contributed equally to all other parts.

Author Information Reprints and permissions information is available at www.nature.com/reprints. The authors declare no competing financial interests. Readers are welcome to comment on the online version of this article at www.nature.com/nature. Correspondence and requests for materials should be addressed to A.R. (arno.rohrbach@gmail.com).

METHODS

Starting material. The starting compositions for multianvil experiments used in this study represent a fertile peridotite composition³⁴ enriched in 5 wt% CO₂ (Supplementary Table 2). Starting composition pyr5 was used to determine the solidus temperature of carbonated peridotite and for runs where the oxygen fugacity of the charge was controlled by the Fe, Ni, and (Au,Ni) capsule materials. Both NiO and CoO contents of pyr5 were set to 1 wt%, to ensure that NiO contents of the phases were high enough for microprobe analysis and f_{O_2} calculation from these data. Experiments using Ir metal as redox sensor were performed with the simplified pyr5 starting material to ensure that the metal phase in the charge is a binary Fe–Ir alloy.

Starting composition pyr5 was prepared from reagent grade oxides SiO₂, TiO₂, Al₂O₃, Cr₂O₃, MgO, fired overnight at 1,000 °C before mixing and grinding under acetone in an agate mortar. Part of the CaO inventory was added to the oxide mix as reagent grade CaCO₃ (dried at 220 °C for 5 h), mixed and decarbonized by stepwise heating to 1,000 °C. Afterwards, iron was added as synthetic fayalite, NiO and CoO as oxides, all dried at 220 °C for 5 h. CO₂ was added as a mixture of reagent grade CaCO₃, MgCO₃ and Na₂CO₃ dried at 220 °C for 5 h in 61/34/5 wt ratio. All components were mixed and ground again thoroughly under acetone in an agate mortar.

Starting composition pyr5 was prepared from reagent grade SiO₂, Al₂O₃, MgO (all fired at 1,000 °C for 5 h) synthetic fayalite, synthetic wollastonite, natural magnesite (kindly provided by P. Ulmer), and reagent grade Na₂CO₃ (all dried at 220 °C for 5 h).

To ensure nominally anhydrous conditions, the starting materials were stored in an desiccator together with silica gel; synthetic rock powders were dried for 2 h at 220 °C before pressing it into capsules and the filled capsule was dried again for 1 h at 220 °C before final welding.

Multianvil experiments. High pressure experiments (Supplementary Table 1) were performed in 600 t and 1,000 t Walker type multianvil devices. We used 32-mm tungsten carbide cubes as second stage anvils and natural pyrophyllite gaskets as pressure transmitting media. We used an 18/11 assembly for runs at 10 GPa (18 mm octahedron edge length, 11 mm truncated edge length), a 14/8 assembly for 14 GPa and a 10/3.5 assembly for 19 and 23 GPa. All assemblies consist of a Cr₂O₃ doped MgO octahedron with LaCrO₃ heater (stepped in case of 18/11 and 14/8), ZrO₂ thermal insulation, MgO spacers, and Mo metal plugs to ensure electrical contact between assembly and WC cubes. Pressure was computer controlled during the entire run; temperature was measured with B- or C-type thermocouples and controlled with a Eurotherm controller to about ±5 °C. Experiments were quenched (by turning off the power supply) at a rate of ~800 °C per second. The total temperature precision including temperature gradients within the capsule might be ±15 °C in 18/11 and 14/8 experiments. Temperature gradients within the 10/3.5 assembly might be 30–50 °C over the capsule length of ~1.2 mm. Details of pressure calibration, design, and temperature gradients of the 10/3.5 assembly are given in ref. 35.

Encapsulation. Runs to determine the carbonated peridotite solidus were performed in welded Au₈₀Pd₂₀ capsules. No attempt was made to control f_{O_2} during these runs. The use of conventional Pt–C double capsules appeared to be problematic as the space is very limited and recovering the sample from the graphite capsule that transformed to diamond during the runs was rather challenging. Mass balance calculations and measured Fe contents in the capsule material show that iron loss from the charge to the Au₈₀Pd₂₀ capsule is negligible (see also X_{Mg} values in Supplementary Table 2).

Runs using Ir metal as redox sensor were performed in welded Au₈₀Pd₂₀ capsules. We added ~10 wt% of graphite to the charges to obtain the f_{O_2} buffering through coexisting C⁰ and carbonate in a peridotite matrix. We added ~5 wt% fine grained Ir metal and 3–5 wt% of metallic Fe to ensure redox equilibrium via carbonate reduction according to reaction (1).

Slightly lower X_{Mg} of all phases in f_{O_2} monitoring runs (Supplementary Table 2) are indicative for reaction (1) and therefore for the attainment of redox equilibrium in these runs. Both diamond and magnesite were present in experimental charges in direct contact with each other as verified by backscattered imaging, EDX and EPMA analysis. This encapsulation method yields results that agree within error to those from experiments in C capsules surrounded by Re metal foil (compare f_{O_2} of runs 39 and 47; Supplementary Table 5) but sample recovery and polishing was facilitated considerably, especially for runs at 23 GPa.

Fe⁰ and Ni⁰ capsules were not welded but cold sealed at run pressure with a conical cap. We added ~3 wt% of the respective metal to the charge to facilitate attainment of equilibrium.

(Au,Ni) alloy capsules were prepared as welded Au outer capsule and Ni foil inner capsule which formed an homogeneous (Au,Ni) alloy at run pressures and temperatures. In runs 22 and 29b we added ~10 wt% NiO in order to raise the NiO content of the phases and accordingly relative f_{O_2} . This NiO-enriched compositions crystallized a NiO-rich periclase instead of ferropericlase at 23 GPa (run 29b) and an olivine enriched in Ni₂SiO₄-component at 14 GPa (run 22, see Supplementary Table 2).

Analytical methods. Recovered sample capsules (in case of 10/3.5 runs, complete octahedra) were mounted in an epoxy resin, ground down with sand paper and polished with polycrystalline diamond paste. Runs to determine the solidus were polished under dry conditions using synthetic polishing paper.

Runs were analysed with a Jeol JXA8200 microprobe using minerals and synthetic oxides as standards. Results are given in Supplementary Table 2. Silicates and oxides were measured at 15 kV and 20 nA with a focused beam, counting times were 20 s on the peak and 10 s on the background. Perovskites and carbonates were measured with an electron beam of 5 µm diameter at 10 nA to minimize radiation damage. Note, however that CaSi-perovskite was still unstable under the beam, which results in low totals. Additionally, CaSi-perovskite often shows a blurred exsolution texture that is difficult to analyse without obtaining mix signals. The majority of the experiments, especially under subsolidus conditions (despite run durations up to 4 days) showed average grain sizes between 3 and 10 µm and did not allow a broad beam. In experiments AR13 and AR18, some phases were too small to be measured by electron microprobe and were identified using backscattered electron images and EDX (Jeol JSM 6390LA scanning electron microscope).

Metals were measured with a focused beam at 15 kV and 20 nA, counting times were 30 s on the peak and 10 s on the background. We used Fe, Ir, Ni and Co metal as standards for quantification to reduce matrix effects. To minimize the excitation volume of the sample, to be able to measure small Ir-Fe alloy grains, we measured Ir at 15 kV and 20 nA using its low excitation energy Mα peak.

Calculation of oxygen fugacities. We calculated f_{O_2} of the experimental charges using Fe–FeO and Ni–NiO redox equilibria. f_{O_2} values are reported relative to iron-wüstite (IW) and nickel–NiO (NNO) buffers. The relative positions of IW and NNO at P and T were calculated after ref. 33, the relative position of the Re–ReO₂ (RRO) buffer was estimated from ref. 36. The activity–composition relationship for (Fe,Ni) alloys were taken from ref. 37, activity data for (Au,Ni) alloys were adopted from ref. 38.

Periclase-bearing experiments. Oxygen fugacities of ferropericlase (fp)-bearing experiments (19 and 23 GPa) were calculated using equilibria of the form



with $M = \text{Fe or Ni}$. f_{O_2} relative to the respective metal–metal oxide (MMO) equilibrium reads:

$$\Delta \log f_{O_2} [\text{MMO}] = 2 \log a_{M}^{\text{fp}} - 2 \log a_{M}^{\text{metal}} \quad (6)$$

where activity (a) is defined as molar fraction (X) times activity coefficient (γ). The molar fraction for metals and phases, calculated activity coefficients and calculated f_{O_2} values of the experiments are summarized in Supplementary Tables 3–5. $a_{\text{FeO}}^{\text{fp}}$ was determined using a binary regular solution model:

$$RT \ln(\gamma_{\text{FeO}}^{\text{fp}}) = (11,000 + 0.011P)(1 - X_{\text{FeO}}^{\text{fp}})^2 \quad (7)$$

for FeO, where P is in bar, T in K, and R is the gas constant³⁹. We note that ferric iron content of ferropericlase was not measured and microprobe FeO^{total} data were used to calculate X_{Fe} . The $\text{Fe}^{3+}/\Sigma\text{Fe}$ for ferropericlase in systems with $X_{\text{Mg}} = 0.9$ however is generally <0.05 (refs 40–42), so calculated f_{O_2} values might therefore be overestimated by a maximum of 0.1 log units.

$a_{\text{NiO}}^{\text{fp}}$ was calculated using a ternary regular solution model for NiO:

$$RT \ln(\gamma_{\text{NiO}}^{\text{fp}}) = W_{\text{Ni-Mg}}(X_{\text{Mg}})^2 + W_{\text{Ni-Mg}}(X_{\text{Fe}})^2 + (W_{\text{Ni-Mg}} + W_{\text{Ni-Fe}} - W_{\text{Mg-Fe}})X_{\text{Mg}} \quad (8)$$

where T is in K, and R is the gas constant^{43,44}.

Olivine-, wadsleyite- or ringwoodite-bearing experiments. f_{O_2} conditions relative to the quartz–fayalite–iron (QFI) equilibrium of runs containing olivine, wadsleyite or ringwoodite (10, 14 and 19 GPa) were calculated using the following expressions:



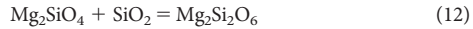
$$\Delta \log f_{O_2} [\text{QFI}] = 2 \log a_{\text{Fe}}^{\text{ol}/\text{wad}/\text{rw}} - 2 \log a_{\text{Fe}}^{\text{metal}} - \log a_{\text{SiO}_2} \quad (10)$$

Activity coefficients were calculated using a binary symmetric solution model where:

$$RT \ln(\gamma_{\text{Fe}}^{\text{ol}}) = W_{\text{Fe-Mg}}^{\text{ol}}(1 - X_{\text{Fe}}^{\text{ol}})^2 \quad (11)$$

Margules parameters including W_V to correct the olivine interaction parameter for pressure were taken from ref. 45 (Supplementary Table 6).

NiO-bearing olivines show a slight negative deviation from ideal mixing, even at the high temperatures relevant for our experiments^{46,47}. Owing to this we set $\gamma_{\text{NiO}}^{\text{ol}} = 0.9$; but the effect on calculated f_{O_2} is minor, that is, in the range ± 0.05 log units. Silica activities (a_{SiO_2}) in experiments containing olivine and clinoenstatite were calculated from the equilibrium:



where

$$\log a_{\text{SiO}_2} = \log a_{\text{en}}^{\text{opx}} - \log a_{\text{fo}}^{\text{ol}} - \log K \quad (13)$$

Enstatite activity in pyroxene was calculated after ref. 48 and forsterite activity in olivine after ref. 45 as described above for fayalite. $\log K$ of reaction (12) was calculated using thermodynamic data⁴⁹. f_{O_2} values relative to IW are obtained by adding the difference in f_{O_2} between QFI and IW equilibria at run P and T to $\Delta \log f_{\text{O}_2}$ [QFI]. **Activity–composition relation in the system Fe–Ir at high P and T .** Iridium metal was used as a redox sensor²⁴ to monitor f_{O_2} in runs that contain both elemental carbon and magnesite between 10 and 23 GPa. Margules interaction parameters (W) dependent on P , T and X are calculated according to the expression

$$W_G = W_{H \text{ 1bar}} - TW_S + (P - 1)W_V \quad (14)$$

where T is in K and P in bar⁵⁰.

$W_{H \text{ 1bar}}$ was obtained by least-squares fitting of a binary asymmetric regular solution model⁵¹ to the non-temperature-dependent part of the excess Gibbs energy (G^{xs}) for face centred cubic (f.c.c.) Ir–Fe alloy⁵². W_S is $-5 \text{ J mol}^{-1} \text{ K}^{-1}$ according to the temperature dependence of the excess Gibbs energy expression for f.c.c. Ir–Fe alloy⁵². W_V is estimated by least-squares fitting of a binary asymmetric regular solution model to excess volumes of the Fe–Ir alloy derived from X-ray data⁵². Activity coefficients γ dependent on P and T , and X values for Fe in f.c.c. Ir–Fe alloy result from a binary asymmetric regular solution model⁵¹:

$$RT \ln(\gamma_{\text{Fe}}^{\text{metal}}) = 2X_{\text{Fe}}X_{\text{Ir}}W_G \text{ Ir-Fe} + (X_{\text{Ir}})^2W_G \text{ Fe-Ir} - 2G^{\text{xs}} \quad (15)$$

where

$$G^{\text{xs}} = X_{\text{Fe}}X_{\text{Ir}}(X_{\text{Ir}}W_G \text{ Fe-Ir} + X_{\text{Fe}}W_G \text{ Ir-Fe}) \quad (16)$$

The effect of correcting the activity model for P and T is shown in Supplementary Fig. 1.

34. Palme, H. & O'Neill, H. St C. in *The Mantle and The Core* Vol 2. (ed. Carlson, R. W.) 1–38 (Elsevier-Pergamon, 2003).

35. Stewart, A. J., van Westrenen, W., Schmidt, M. W. & Melekhova, E. Effect of gasketing and assembly design: a novel 10/3.5 mm multi-anvil assembly reaching perovskite pressures. *High Press. Res.* **26**, 293–299 (2006).
36. Campbell, A. J. et al. Pressure–volume–temperature studies of metal–oxide pairs. In *COMPRES Annual Meeting* (2007); (www.geol.umd.edu/~ajc/Posters/CampbellCOMPRES2007poster.pdf).
37. Predel, B. Fe–Ni in *The Landolt–Börnstein Database* (ed. Madelung, O.) (Springer Materials, 1995); doi:10.1007/10474837_1321.
38. Wang, J., Lu, X.-G., Sundman, B. & Su, X. Thermodynamic assessment of the Au–Ni system. *Comput. Coupling Phase Diagr. Thermochem.* **29**, 263–268 (2005).
39. Frost, D. J. Fe²⁺–Mg partitioning between garnet, magnesiowüstite and (Mg,Fe)₂SiO₄ phases of the transition zone. *Am. Mineral.* **88**, 387–397 (2003).
40. McCammon, C. A., Peyronneau, J. & Poirier, J.-P. Low ferric iron content of (Mg,Fe)O at high pressures and temperatures. *Geophys. Res. Lett.* **25**, 1589–1592 (1998).
41. Frost, D. J., Langenhorst, F. & van Aken, P. Fe–Mg partitioning between ringwoodite and magnesiowüstite and the effect of pressure, temperature and oxygen fugacity. *Phys. Chem. Miner.* **28**, 455–470 (2001).
42. Frost, D. J. & Langenhorst, F. The effect of Al₂O₃ on Fe–Mg partitioning between magnesiowüstite and magnesium silicate perovskite. *Earth Planet. Sci. Lett.* **199**, 227–241 (2002).
43. Seifert, S. & O'Neill, H. St C. Experimental determination of activity–composition relations in Ni₂SiO₄–Mg₂SiO₄ and Co₂SiO₄–Mg₂SiO₄ olivine solid solutions at 1200 K and 0.1 MPa and 1573 K and 0.5 GPa. *Geochim. Cosmochim. Acta* **51**, 97–104 (1987).
44. O'Neill, H., St. C., Canil, D. & Rubie, D. C. Oxide metal equilibria to 2500 °C and 25 GPa: implications for core formation and the light component in the Earth's core. *J. Geophys. Res.* **103**, 12239–12260 (1998).
45. Frost, D. J. The structure and sharpness of (Mg,Fe)₂SiO₄ phase transformations in the transition zone. *Earth Planet. Sci. Lett.* **216**, 313–328 (2003b).
46. Hirschmann, M. Thermodynamics of multicomponent olivines and the solution properties of (Ni,Mg,Fe)₂SiO₄ and (Ca,Mg,Fe)₂SiO₄ olivines. *Am. Mineral.* **76**, 1232–1248 (1991).
47. Hirschmann, M. M. & Ghiorso, M. S. Activities of nickel, cobalt and manganese silicate in magmatic liquids and application to olivine/liquid and to silicate/melt partitioning. *Geochim. Cosmochim. Acta* **58**, 4109–4126 (1994).
48. O'Neill, H. S. C. & Wall, V. J. The olivine–orthopyroxene–spinel oxygen geobarometer, the nickel precipitation curve, and the oxygen fugacity of the Earth's upper mantle. *J. Petrol.* **28**, 1169–1191 (1987).
49. Barin, I., Sauerb, F., Schultze-Rhonhof, E. & Sheng, W. S. *Thermochemical Data of Pure Substances* Parts I and II (Weinheim, 1989).
50. Wood, B. J. & Fraser, D. G. *Elementary Thermodynamics for Geologists* (Oxford Univ. Press, 1976).
51. Mukhopadhyay, B., Basu, S. & Holdaway, M. J. A discussion of Margules-type formulations for multicomponent solutions with a generalized approach. *Geochim. Cosmochim. Acta* **57**, 277–283 (1993).
52. Swartzendruber, L. J. The Fe–Ir (iron–iridium) system. *Bull. Alloy Phase Diagrams* **5**, 48–52 (1984).